








RESEARCH ARTICLE | SEPTEMBER 01 2023

Broadband surface-emitting THz laser frequency combs with inverse-designed integrated reflectors

Urban Senica ; Sebastian Gloor ; Paolo Micheletti ; David Stark ; Mattias Beck ; Jérôme Faist ; Giacomo Scalari 

 Check for updates

APL Photonics 8, 096101 (2023)
<https://doi.org/10.1063/5.0163337>



CrossMark

21 January 2024 20:27:21

AIP Advances

Why Publish With Us?



25 DAYS
average time
to 1st decision



740+ DOWNLOADS
average per article



INCLUSIVE
scope

[Learn More](#)



Broadband surface-emitting THz laser frequency combs with inverse-designed integrated reflectors

Cite as: APL Photon. 8, 096101 (2023); doi: 10.1063/5.0163337
Submitted: 16 June 2023 • Accepted: 11 August 2023 •
Published Online: 1 September 2023



Urban Senica,^{a)}  Sebastian Gloor,  Paolo Micheletti,  David Stark,  Mattias Beck,  Jérôme Faist, 
and Giacomo Scarlari^{a)} 

AFFILIATIONS

Quantum Optoelectronics Group, Institute of Quantum Electronics, ETH Zürich, 8093 Zürich, Switzerland

^{a)} Authors to whom correspondence should be addressed: usenica@phys.ethz.ch and scarlari@phys.ethz.ch

ABSTRACT

THz quantum cascade lasers (QCLs) based on double metal waveguides feature broadband and high-temperature devices for their use in spectroscopy and sensing. However, their extreme field confinement produces poor output coupling efficiencies and divergent far-fields. Here, we present a planarized THz QCL with an inverse-designed end facet reflector coupled to a surface-emitting patch array antenna. All the components have been optimized for octave-spanning spectral bandwidths between 2 and 4 THz and monolithically integrated on the same photonic chip. We demonstrate this experimentally on broadband THz QCL frequency combs, with measured devices showing a seven-fold improvement in slope efficiency compared to devices with a cleaved facet. They feature a peak power of up to 13.5 mW with surface emission into a narrow beam with a divergence of $(17.0^\circ \times 18.5^\circ)$, while broadband fundamental and harmonic comb states spanning up to 800 GHz are observed.

© 2023 Author(s). All article content, except where otherwise noted, is licensed under a Creative Commons Attribution (CC BY) license (<http://creativecommons.org/licenses/by/4.0/>). <https://doi.org/10.1063/5.0163337>

INTRODUCTION

THz quantum cascade laser (QCL)¹ frequency combs² and dual combs³ are compact sources of coherent THz radiation, promising for use in broadband spectroscopy and sensing. Recent milestones in the field of THz QCLs include high-temperature operation with thermoelectric coolers,^{4–6} comb and soliton formation in ring cavities,^{7,8} operation as fast THz detectors,^{9,10} and planarized waveguides for integrated THz photonics.¹¹

However, a major practical limitation of broadband THz QCL frequency comb devices has been their low output powers and poor far-field patterns. Both properties originate from the double metal waveguide cavity configuration. Since the propagating optical mode is confined to subwavelength dimensions (typically, $d \sim 10 \mu\text{m}$ for a central emission wavelength of $\lambda_0 \sim 100 \mu\text{m}$), it acts as a point-like source and produces highly divergent and frequency-dependent far-field patterns. In addition, due to metallic waveguide confinement and the resulting large impedance mismatch between the guided

and free space optical modes, the facet reflectivities are relatively high, in the order of $R = 70\%$ at a frequency of 3 THz. While this does reduce the mirror losses, it also limits the slope efficiencies and output powers. There have been a variety of approaches to improve the outcoupling properties of THz QCLs, but these have either been optimized for narrowband emission,^{12,13} have an intrinsically limited bandwidth,^{14,15} or require additional post-processing and mounting steps.^{16,17}

Here, we use inverse-designed end facet reflectors for precise control of the mirror losses and output power, and couple the optical mode to a surface-emitting patch array antenna, all monolithically integrated on the same photonic chip, as shown in Fig. 1. All the designed components have been optimized for an octave-spanning emission spectrum between 2 and 4 THz and improve the output power and far-field pattern while featuring broadband comb states simultaneously. The presented devices are based on our recently developed planarized waveguide platform,¹¹ where the active waveguides (with a copper-copper metallic cladding) are embedded in

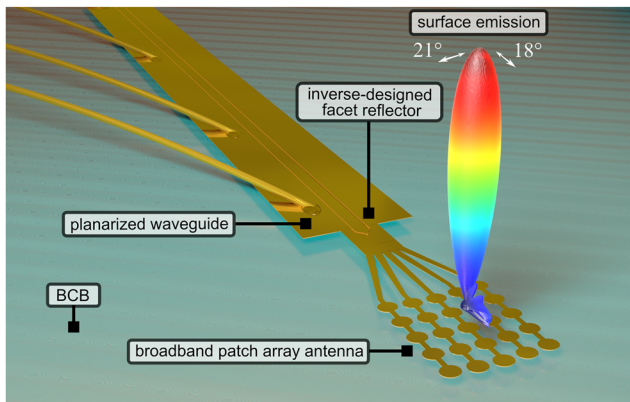


FIG. 1. Illustration of the fabricated device: on the front side of a planarized ridge waveguide is an inverse-designed end facet reflector, which is coupled to a passive waveguide connecting to a broadband patch array antenna for surface emission. A spherical plot of the simulated broadband far-field pattern is superimposed on top of the antenna structure [same as in Fig. 3(b), where the measured emission spectrum is included in the far-field simulation]. The emitted light is linearly polarized (aligned with the ridge waveguide).

RESULTS

Inverse-designed end facet reflectors

We first address the limited output powers due to the high reflectivity of the cleaved end facets of double metal waveguides.¹⁸ In our recent work, we have shown that the planarized waveguide platform enables the reduction of end facet reflectivities by coupling the active waveguide into a passive waveguide, defined with a metallic stripe on the top of the surrounding lower refractive index material (BCB, $n = 1.57$).¹¹ In the simplest configuration, a flat dry-etched planarized facet results in a reduced reflectivity of around $R = 23\%$ at a frequency of 3 THz in the passive waveguide. This is already a remarkable reduction with respect to a cleaved facet value of 70%.

In order to have precise control of the facet reflectivity over a broad bandwidth, we implemented an inverse design approach based on adjoint optimization.¹⁹ In recent years, inverse design has emerged as a powerful design and optimization tool in various areas and applications in photonics.²⁰ The main advantage of such an approach is that instead of manual parameter sweeps and fine-tuning to achieve a high-performance device design, an optimization algorithm is used to adapt the structure in an iterative loop to maximize the desired figure of merit automatically.

In our specific geometry, we implemented an inverse-design shape optimization simulation loop, where the outline shape of the end facet is modified to match the desired reflectivity value. As the optimization converges to a local optimum, the initial structure is crucial as well (we used a tapered edge shape). More details on the parametrization and implementation can be found

a low-loss polymer, Benzocyclobutene (BCB), and an extended top metallization is defined, which improves the waveguide properties and enables the fabrication of passive structures on the same photonic chip.

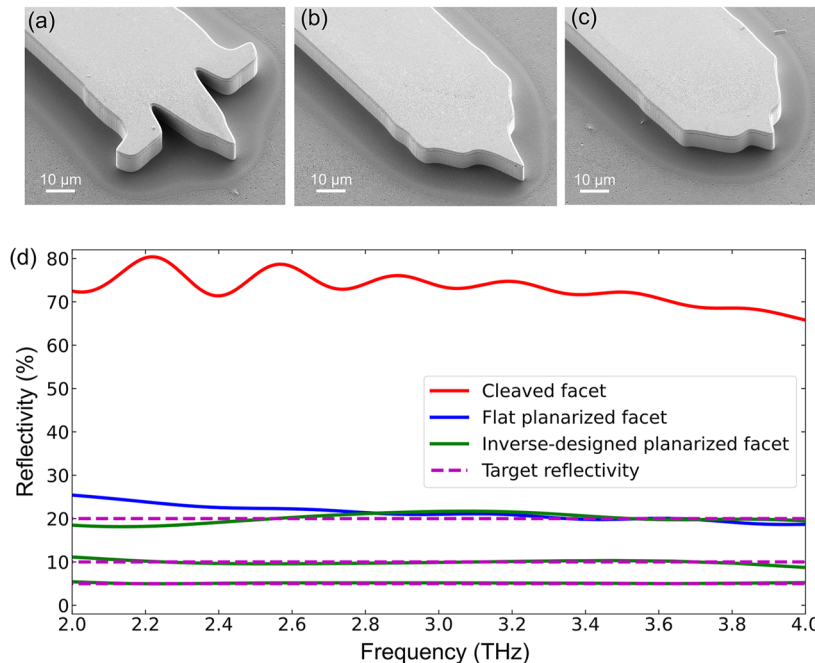


FIG. 2. (a)–(c) SEM images of the dry-etched inverse-designed facet reflectors with designed facet reflectivities of 5%, 10%, and 20%, respectively. Subsequently, the waveguides are planarized with BCB, and an extended top metallization and antenna extractor are deposited. (d) Simulated reflectivities of a cleaved facet, a flat planarized facet, and the inverse-designed planarized facets, where the simulated reflectivities match well with the target reflectivities.

in the supplemental material. Due to the symmetric planarized waveguide structure, only a 2D slice of the structure and an in-plane (x - y , perpendicular to the growth direction z of the heterostructure) propagation simulation are required. In addition, the adjoint optimization approach features very fast convergence, as it only requires two simulations of the current structure geometry (a forward and a backward propagation simulation) to compute the gradients and update all the geometrical parameters in a single step. These favorable aspects result in a very efficient optimization routine that produces optimized designs after only around 25 iterations, taking less than an hour on a normal desktop computer.

In Figs. 2(a)–2(c), we show SEM images of fabricated dry-etched inverse-designed end facets, designed to have a 5%, 10%, and 20% reflectivity over octave-spanning spectra between 2 and 4 THz. Subsequently, the active waveguides are planarized with a low-loss polymer BCB, and the top metallization is defined (see Ref. 11 for details).

A comparison between the simulated reflectivities of cleaved, flat planarized, and inverse-designed planarized facets is shown in Fig. 2(d). The facets do not induce any considerable group delay in dispersion after reflection, which could otherwise be detrimental to comb formation.

Surface-emitting patch array antenna

After a partial reflection at the planarized end facet, the optical mode is guided within a passive waveguide and coupled into a surface-emitting patch array antenna. As the propagating light wave spreads out into the antenna branches, the individual patches oscillate in phase and combine into a narrow vertical beam. The basic design intended for single-mode operation was presented in Ref. 13.

Here, we developed a broadband patch array antenna, shown in the optical microscope image in Fig. 3(a). This design has also been optimized for octave-spanning emission spectra, matching the same broad frequency range as the reflector structures. First, to reduce the beam divergence, the antenna emission area was enlarged by increasing the number of patch elements to (5×5) . For broadband emission, the optimal shape, size, and positioning of the individual antenna elements were found with full-wave numerical simulations of the surface emission, where a minimal beam divergence and beam steering with frequency were obtained. In particular, since the light is coupled into the antenna from one side, the element spacing needs to be such that the patch elements oscillate in phase and produce a beam in the vertical direction, which was tuned to a central emission frequency of 2.9 THz. For a detuned frequency, there is a small phase

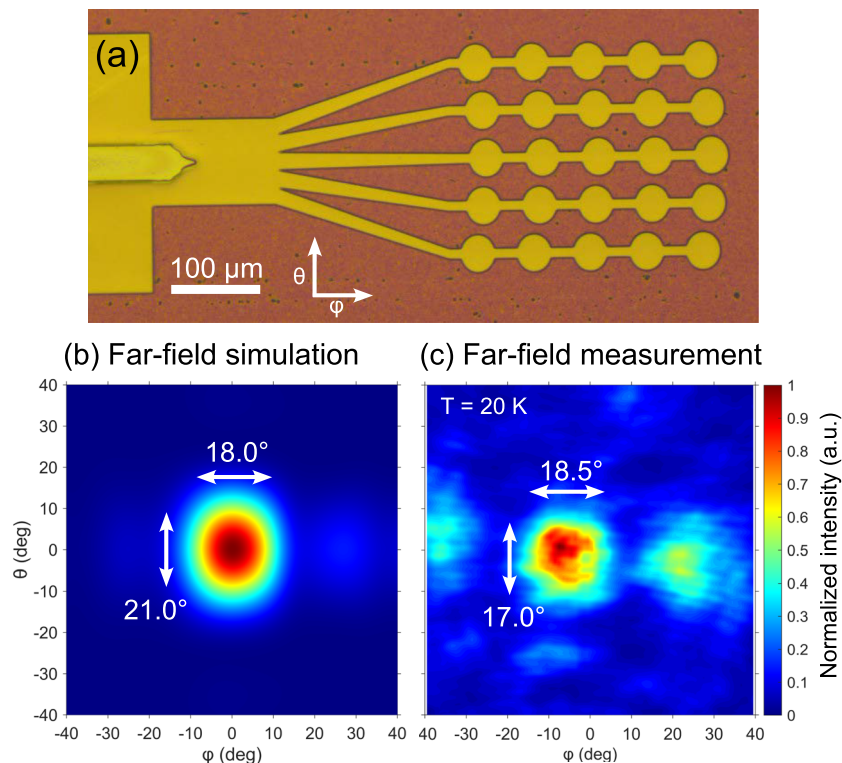


FIG. 3. (a) Optical microscope image of the front side of a planarized ridge waveguide, where an inverse-designed facet reflector is coupled via a passive waveguide into a broadband patch array antenna for surface emission. (b) Broadband far-field simulation, which uses the emission spectrum of the measured device, produces a single-lobed pattern. (c) Far-field measurement of a broadband device agrees well with the simulation with a FWHM beam width of $(17.0^\circ \times 18.5^\circ)$.

shift between the elements, which results in a slight tilt of the beam direction (however, this effect was not significant). The appropriate element size is chosen to produce a radiative field component, while the elliptical shape results in a broadband response, i.e., a significant radiative field component over a broad frequency range. Combining all these aspects results in an ultra-broadband surface emission in a narrow beam.

In Fig. 3(b), we show the simulated broadband far-field pattern, which features a single narrow lobe in the vertical emission direction. The result was obtained by including the emission spectrum of the measured device with frequency-dependent far-field simulation results. Specifically, this was done with a spectrally weighted linear sum of simulated far-field patterns, as described in more detail in Ref. 17.

The antenna far-field measurement in Fig. 3(c) agrees well with the simulations with a full-width half-maximum (FWHM) beam divergence of $(17.0^\circ \times 18.5^\circ)$. The measurement was performed on a broadband emission sample using a pyroelectric detector (Gentec-EO: THZ2I-BL-BNC) mounted on a motorized angular scanning stage. The laser was driven in the micro-pulse (500-ns-long pulses, 20% duty cycle), macro-pulse mode (30 Hz, 50% duty cycle), where the emission spectrum was spanning between around 2.3–3.3 THz.

High-power surface emission

With a reduction of the front end facet reflectivity R_1 , the mirror losses are increased through the relation

$$\alpha_m = -\frac{1}{2L} \ln(R_1 R_2), \quad (1)$$

where L is the waveguide length and R_2 is the back mirror reflectivity. On the one hand, together with waveguide losses α_{wg} , this increases the total losses $\alpha_{tot} = \alpha_{wg} + \alpha_m$ with an expected increase in the lasing threshold. On the other hand, the slope efficiency²¹ should be increased, as follows:

$$\frac{dP}{dI} = \frac{N_p h \nu}{e} \frac{\alpha_{m,1}}{\alpha_{tot}} \frac{\tau_{eff}}{\tau_{eff} + \tau_2}. \quad (2)$$

When comparing different devices fabricated using the same active region, only the $\frac{\alpha_{m,1}}{\alpha_{tot}}$ ratio is changing.

To evaluate the performance of the inverse-designed end facet reflectors, we experimentally compare three different front (extracting) facets of devices processed on the same chip. These are a cleaved facet, a flat planarized facet with the antenna, and a 10% reflectivity inverse-designed planarized facet with the antenna. The first one has a high-reflectivity back facet and a total length of 2.8 mm, while both antenna samples have a cleaved back facet and a length of 2.5 mm. All the samples have the same active waveguide width of 40 μm to ensure the same waveguide loss α_{wg} and nearly the same total active device area (a difference of <5%).

In Fig. 4(a), we plot the measured LJV curves of the three devices, all characterized under the same operating conditions (a heat sink temperature of 20 K, 500 ns pulses, and a duty cycle of 20%). The output power was measured by using a large area calibrated absolute power meter (Thomas Keating Ltd.), which ensures the whole THz emission is collected (even in the case of poor

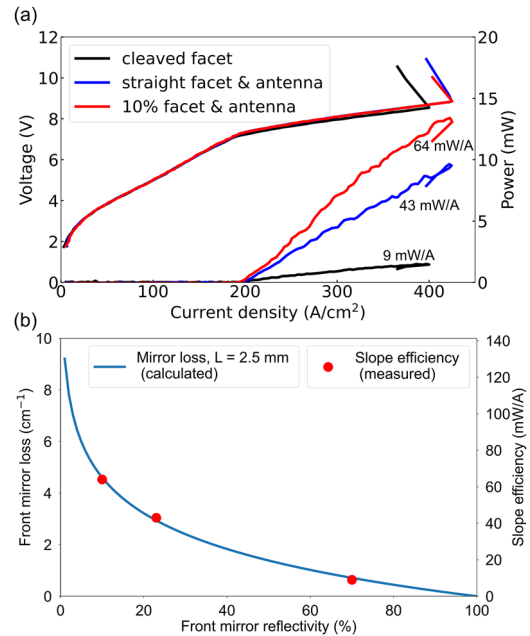


FIG. 4. (a) LJV curves comparison of devices with a cleaved facet, a flat planarized facet, and a 10% reflectivity inverse-designed facet. While the threshold current density increases only slightly, the output power and slope efficiency increase significantly with planarized facets and an antenna. (b) Calculated front mirror loss for the different measured facets (the blue line is for a cavity length of 2.5 mm). The red dots mark the measured slope efficiencies, which follow the same dependence with a varying front mirror reflectivity.

far-field patterns of cleaved facets). When measuring the THz emission within a narrower range of spatial angles (typical for spectroscopy experiments), the improved collection efficiency due to the antenna would result in an even more favorable ratio of slope efficiencies. The comparison of calculated and experimental results for the three devices is summarized in Table I.

TABLE I. Summary of an experimental comparison of three different types of laser waveguide end facets.

Parameter	Cleaved facet	Flat facet	10% facet
R_1 (%)	70	23	10
Length (mm)	2.8	2.5	2.5
I_{thr} (mA)	178	195	195
J_{thr} (A/cm²)	185	195	195
$\alpha_{m,1}$ (cm⁻¹)	0.64	2.94	4.61
α_{tot} (cm⁻¹)	20.6	23.7	25.3
$\frac{dP}{dI}$ (mW/A)	9	43	64
P_{max} (mW)	1.5	9.5	13.5
$\alpha_{m,1}$ ratio	1	4.6	7.2
$\frac{dP}{dI}$ ratio	1	4.8	7.1

When replacing the front cleaved facet with a planarized antenna-coupled facet, the threshold current density J_{thr} only increases slightly (from 185 to 195 A/cm²). This suggests that for such waveguide lengths ($L = 2.5$ mm and longer), the total losses are dominated by waveguide losses. Indeed, the waveguide losses of double metal waveguides are estimated to be in the order of 20 cm⁻¹ (due to the overlap with lossy metals, intersubband absorption, and scattering losses from sidewall roughness), while the computed front mirror losses are below 5 cm⁻¹ for all the considered types of facets. In such a case, the comparison of slope efficiencies can be simplified from $\frac{dP}{dI} \propto \frac{\alpha_{m,1}}{\alpha_{\text{wg}} + \alpha_m}$ to $\frac{dP}{dI} \propto \alpha_{m,1}$. In Fig. 4(b), we plot the calculated front mirror loss (blue line) and the measured slope efficiencies (red dots). As these follow the same dependence vs the front mirror reflectivity, we are indeed in a regime where waveguide losses dominate over mirror losses. The measured slope efficiency of 64 mW/A of the sample with the 10% inverse-designed facet and the antenna is a factor of 7.1 higher than for the cleaved facet reference sample, with a measured peak power of 13.5 mW. We should also note here that while reducing the reflectivity to even lower values (close to $R_1 = 0\%$) is tempting in terms of predicted slope efficiencies, the quickly increasing mirror losses would start to increase the laser threshold significantly, eventually preventing lasing.

Broadband frequency combs

After demonstrating the improved far-field and outcoupling efficiency properties, we now highlight the broadband frequency comb performance. In general, the comb locking formation and spectral bandwidth in QCLs are a result of an interplay of several effects, such as chromatic dispersion, Kerr nonlinearity with four-wave mixing, spatial hole burning, gain curvature, and self- and cross-steepening nonlinearities, as is discussed in more detail in Refs. 22–24. The results of extensive comb simulations presented in Refs. 25 and 26 suggest that a reduced end facet reflectivity increases the cross-steepening nonlinearity due to a larger field discontinuity at the end facet, which could produce broader comb spectra. The ability to design the end facet reflectivity presented in this work introduces a new tuning knob for achieving high-performance comb operation (the optimal facet reflectivity for the broadest bandwidth will most likely vary between devices, predominantly depending on the active region properties).

In Fig. 5, we show the measured THz and RF spectra of the 10% reflectivity inverse-designed facet device from the previous section (length $L = 2.5$ mm and width $w = 40$ μm). The device was operated in continuous wave (CW) at a heat sink temperature of 30 K. In panel (a), we show a free-running fundamental comb spanning around 800 GHz with a single strong RF beatnote at a roundtrip frequency of $f_{\text{rep}} = 15.4$ GHz. Free-running harmonic comb states^{27–29} are observed as well, where the mode spacing is an integer multiple of f_{rep} . A free-running second harmonic comb spanning around 750 GHz is shown in panel (b), with a single RF beatnote at $2f_{\text{rep}}$. With the changed cavity boundary conditions, the time domain properties^{3,30,31} of these comb states are of high interest for future systematic studies, where the facet reflectivity will be varied and its impact on comb dynamics will be elucidated, in combination with simulations of comb formation in Fabry–Pérot THz QCLs.²⁹

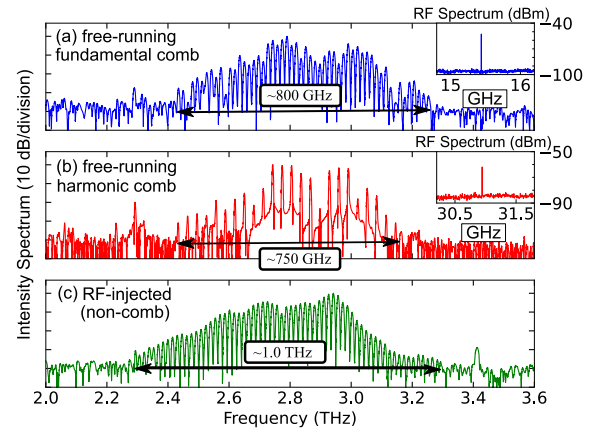


FIG. 5. Measured THz and RF spectrum of the 10% reflectivity inverse-designed facet device in CW at a heat sink temperature of 30 K. (a) Free-running fundamental comb spanning 800 GHz and a strong single RF beatnote at the roundtrip frequency of $f_{\text{rep}} = 15.4$ GHz. (b) Free-running second harmonic comb spanning 750 GHz and a strong single RF beatnote at $2f_{\text{rep}} = 30.8$ GHz. (c) Strongly RF-injected (+32 dBm at source) incoherent state spanning around 1 THz.

By injecting a strong RF signal into the laser cavity, the emission can be further broadened. Experimentally, we observe two different regimes. When the injected RF signal is close to the free-running comb beatnote, we can injection-lock it to stabilize the comb and also induce some spectral broadening.^{32,33} To obtain the broadest emission spectrum, both the RF power is increased significantly (>20–30 dBm at the source) and the injection frequency is detuned from the repetition rate (by as much as 100–200 MHz). This does not produce a coherent injection-locked state but very broadband emission with an off-resonant RF injection, as shown in Fig. 5(c), with similar experimental results shown already in Refs. 11 and 34. The incoherent property of the state is apparent from an asymmetric and decaying interferogram after an FTIR measurement. With such strong RF injection, the induced bias voltage swing most likely results in the laser periodically switching between the stable and NDR (unstable) regimes, which results in a significant spectral broadening. The latter is also related to the specific type of active region design used, which features a highly diagonal radiative transition in real space and bistability in the NDR region, as is discussed in more detail in Refs. 34 and 35. An unlocked (incoherent) state with a strong RF injection was also predicted in simulations in Refs. 36 and 37.

CONCLUSION

In conclusion, we have presented a new, high-performance planarized THz quantum cascade laser geometry where inverse-designed end facet reflectors coupled to surface-emitting antennas result in a seven-fold improvement of the slope efficiency. All the components are optimized for octave-spanning emission spectra, and the measured far-field patterns of broadband devices feature a FWHM beam divergence of $(17.0^\circ \times 18.5^\circ)$. The devices operate as broadband frequency combs spanning 800 GHz, with a peak power as high as 13.5 mW. Since the end facet reflectors and antenna are separated by a passive waveguide, we have decoupled the laser

mirror reflectivities and the outcoupling structure, allowing for independent control of both aspects.

Moreover, by further reducing the mirror reflectivities and improving the output beam quality, external cavity^{38,39} broadband THz QCLs could be fabricated, where the comb repetition rate is continuously tunable by an external mirror/grating. In principle, a near-zero reflectivity end facet can be fabricated by an adiabatic tapered transition between the active and passive waveguides, facilitating the lasing operation on external cavity modes. The numerical simulation results of such a structure are shown in the supplemental material, where a modal reflectivity of below $\sim 0.3\%$ is obtained for frequencies between 2 and 4 THz. In contrast to THz QC-VECSELS,^{40,41} comb operation should be more easily obtained as the planarized ridge waveguide can naturally provide both a broad gain and many longitudinal lasing modes.

It is important to emphasize that the presented device is a general layout that can be used with any type of THz QCL active material to engineer the far-field properties and enhance the outcoupling efficiency with a planar and monolithic fabrication technology. In recent years, substantial progress has been made in the field of high-power and high-temperature devices, both in simulations^{42–46} and experiments.^{4–6} In combination with high-performance epilayers, such as the ones presented in Refs. 4 and 5, the peak powers of simple ridge devices at low temperatures could easily go into the Watt-level range while simultaneously being directed into a narrow beam due to the antenna. On the other hand, the output power typically reduces significantly as the temperature is increased. In addition, in this case, the improved output power and beam properties are beneficial and could facilitate the development of improved portable sensing schemes with thermoelectric coolers at temperatures above 200 K.⁵

Finally, in some cases, the total losses (including the mirror losses) need to be minimized (e.g., at very low⁴⁷ or high⁴⁸ emission frequencies), while a high-quality beam is still desired. With our planarized geometry, it is possible to design a facet with high reflectivity where the remaining fraction of the light is coupled to the patch array antenna. In the supplemental material, we added simulation studies for a simple approach: a leaky distributed Bragg reflector (DBR), where a reduced number of periods can be used to tune the facet reflectivities to 70% and above (a similar DBR structure can be implemented on the back laser facet to reduce mirror losses and increase the output power).

SUPPLEMENTARY MATERIAL

More details on the implementation of the inverse design approach along with the structure parameterization and an example optimization run with the simulation outputs (i.e., the figure of merit, updated geometry, electromagnetic field profiles and the evolution of the parameters) can be found in the supplemental material. Additionally, simulation studies of structures with near-zero reflectivity for external cavity experiments as well as high reflectivities for low losses are also shown and discussed.

ACKNOWLEDGMENTS

The authors gratefully acknowledge funding from the ERC Grant CHIC (Grant No. 724344) and in part from the SNF MINT

Project Nos. 200021–212735, and the EU project iFLOWS (Grant No. 101057844).

AUTHOR DECLARATIONS

Conflict of Interest

The authors have no conflicts to disclose.

Author Contributions

Urban Senica: Conceptualization (lead); Data curation (lead); Formal analysis (lead); Investigation (lead); Methodology (lead); Software (lead); Writing – original draft (lead); Writing – review & editing (lead). **Sebastian Gloor:** Data curation (equal); Formal analysis (equal); Investigation (equal); Methodology (equal); Software (equal); Writing – review & editing (equal). **Paolo Micheletti:** Investigation (equal); Methodology (equal); Writing – review & editing (equal). **David Stark:** Investigation (equal); Methodology (equal); Writing – review & editing (equal). **Mattias Beck:** Investigation (supporting); Methodology (supporting); Writing – review & editing (equal). **Jérôme Faist:** Project administration (equal); Resources (equal); Supervision (equal); Writing – review & editing (equal). **Giacomo Scalari:** Conceptualization (equal); Funding acquisition (lead); Project administration (lead); Resources (equal); Supervision (lead); Writing – original draft (supporting); Writing – review & editing (equal).

DATA AVAILABILITY

The data that support the findings of this study are available from the corresponding authors upon reasonable request.

REFERENCES

- R. Köhler, A. Tredicucci, F. Beltram, H. E. Beere, E. H. Linfield, A. G. Davies, D. A. Ritchie, R. C. Iotti, and F. Rossi, “Terahertz semiconductor-heterostructure laser,” *Nature* **417**, 156–159 (2002).
- D. Burghoff, T.-Y. Kao, N. Han, C. W. I. Chan, X. Cai, Y. Yang, D. J. Hayton, J.-R. Gao, J. L. Reno, and Q. Hu, “Terahertz laser frequency combs,” *Nat. Photonics* **8**, 462–467 (2014).
- M. Rösch, G. Scalari, G. Villares, L. Bosco, M. Beck, and J. Faist, “On-chip, self-detected terahertz dual-comb source,” *Appl. Phys. Lett.* **108**, 171104 (2016).
- L. Bosco, M. Franckić, G. Scalari, M. Beck, A. Wacker, and J. Faist, “Thermoelectrically cooled THz quantum cascade laser operating up to 210 K,” *Appl. Phys. Lett.* **115**, 010601 (2019).
- A. Khalatpour, A. K. Paulsen, C. Deimert, Z. R. Wasilewski, and Q. Hu, “High-power portable terahertz laser systems,” *Nat. Photonics* **15**, 16 (2021).
- A. Khalatpour, M. C. Tam, S. J. Addamane, J. Reno, Z. Wasilewski, and Q. Hu, “Enhanced operating temperature in terahertz quantum cascade lasers based on direct phonon depopulation,” *Appl. Phys. Lett.* **122**, 161101 (2023).
- M. Jaidl, N. Opačak, M. A. Kainz, S. Schönhuber, D. Theiner, B. Limbacher, M. Beiser, M. Giparakis, A. M. Andrews, G. Strasser *et al.*, “Comb operation in terahertz quantum cascade ring lasers,” *Optica* **8**, 780–787 (2021).
- P. Micheletti, U. Senica, A. Forrer, S. Cibella, G. Torrioli, M. Frankić, M. Beck, J. Faist, and G. Scalari, “Terahertz optical solitons from dispersion-compensated antenna-coupled planarized ring quantum cascade lasers,” *Sci. Adv.* **9**, eadf9426 (2023).
- P. Micheletti, J. Faist, T. Olariu, U. Senica, M. Beck, and G. Scalari, “Regenerative terahertz quantum detectors,” *APL Photonics* **6**, 106102 (2021).

- ¹⁰V. Pistore, E. A. A. Pogna, L. Viti, L. Li, A. G. Davies, E. H. Linfield, and M. S. Vitiello, "Self-induced phase locking of terahertz frequency combs in a phase-sensitive hyperspectral near-field nanoscope," *Adv. Sci.* **9**, 2200410 (2022).
- ¹¹U. Senica, A. Forrer, T. Olariu, P. Micheletti, S. Cibella, G. Torrioli, M. Beck, J. Faist, and G. Scalari, "Planarized THz quantum cascade lasers for broadband coherent photonics," *Light: Sci. Appl.* **11**, 347 (2022).
- ¹²M. I. Amanti, M. Fischer, G. Scalari, M. Beck, and J. Faist, "Low-divergence single-mode terahertz quantum cascade laser," *Nat. Photonics* **3**, 586–590 (2009).
- ¹³L. Bosco, C. Bonzon, K. Ohtani, M. Justen, M. Beck, and J. Faist, "A patch-array antenna single-mode low electrical dissipation continuous wave terahertz quantum cascade laser," *Appl. Phys. Lett.* **109**, 201103 (2016).
- ¹⁴M. Rösch, I.-C. Benea-Chelmsu, C. Bonzon, M. J. Süess, M. Beck, J. Faist, and G. Scalari, "Broadband monolithic extractor for metal-metal waveguide based terahertz quantum cascade laser frequency combs," *Appl. Phys. Lett.* **111**, 021106 (2017).
- ¹⁵X. Xu and Z. Wang, "Thermal conductivity enhancement of benzocyclobutene with carbon nanotubes for adhesive bonding in 3-D integration," *IEEE Trans. Compon., Packag., Manuf. Technol.* **2**, 286–293 (2012).
- ¹⁶A. Wei Min Lee, Q. Qin, S. Kumar, B. S. Williams, Q. Hu, and J. L. Reno, "High-power and high-temperature THz quantum-cascade lasers based on lens-coupled metal-metal waveguides," *Opt. Lett.* **32**, 2840–2842 (2007).
- ¹⁷U. Senica, E. Mavrona, T. Olariu, A. Forrer, M. Shahmohammadi, M. Beck, J. Faist, and G. Scalari, "An antipodal Vivaldi antenna for improved far-field properties and polarization manipulation of broadband terahertz quantum cascade lasers," *Appl. Phys. Lett.* **116**, 161105 (2020).
- ¹⁸B. S. W. S. Kohan and Q. Hu, "Electromagnetic modeling of terahertz quantum cascade laser waveguides and resonators," *J. Appl. Phys.* **97**, 053106 (2005).
- ¹⁹C. M. Lalau-Keraly, S. Bhargava, O. D. Miller, and E. Yablonovitch, "Adjoint shape optimization applied to electromagnetic design," *Opt. Express* **21**, 21693 (2013).
- ²⁰S. Molesky, Z. Lin, A. Y. Piggott, W. Jin, J. Vucković, and A. W. Rodriguez, "Inverse design in nanophotonics," *Nat. Photonics* **12**, 659–670 (2018).
- ²¹J. Faist, *Quantum Cascade Lasers*, 1st ed. (Oxford University Press, Oxford, United Kingdom, 2013).
- ²²N. Opačak and B. Schwarz, "Theory of frequency-modulated combs in lasers with spatial hole burning, dispersion, and Kerr nonlinearity," *Phys. Rev. Lett.* **123**, 243902 (2019).
- ²³D. Burghoff, "Unraveling the origin of frequency modulated combs using active cavity mean-field theory," *Optica* **7**, 1781–1787 (2020).
- ²⁴C. Silvestri, X. Qi, T. Taimre, K. Bertling, and A. D. Rakić, "Frequency combs in quantum cascade lasers: An overview of modeling and experiments," *APL Photonics* **8**, 020902 (2023).
- ²⁵L. Humbarud and D. Burghoff, "Analytical theory of frequency-modulated combs: Generalized mean-field theory, complex cavities, and harmonic states," *Opt. Express* **30**, 5376–5401 (2022).
- ²⁶M. Beiser, N. Opačak, J. Hillbrand, G. Strasser, and B. Schwarz, "Engineering the spectral bandwidth of quantum cascade laser frequency combs," *Opt. Lett.* **46**, 3416–3419 (2021).
- ²⁷D. Kazakov, M. Piccardo, Y. Wang, P. Chevalier, T. S. Mansuripur, F. Xie, C.-e. Zah, K. Lascola, A. Belyanin, and F. Capasso, "Self-starting harmonic frequency comb generation in a quantum cascade laser," *Nat. Photonics* **11**, 789 (2017).
- ²⁸A. Forrer, Y. Wang, M. Beck, A. Belyanin, J. Faist, and G. Scalari, "Self-starting harmonic comb emission in THz quantum cascade lasers," *Appl. Phys. Lett.* **118**, 131112 (2021).
- ²⁹U. Senica, A. Dikopoltsev, A. Forrer, S. Cibella, G. Torrioli, M. Beck, J. Faist, and G. Scalari, "Frequency-modulated combs via on-chip field enhancement," *arXiv:2305.01483* [physics.optics] (2023).
- ³⁰F. Cappelli, L. Consolino, G. Campo, I. Galli, D. Mazzotti, A. Campa, M. Siciliani de Cumis, P. Cancio Pastor, R. Eramo, M. Rösch *et al.*, "Retrieval of phase relation and emission profile of quantum cascade laser frequency combs," *Nat. Photonics* **13**, 562–568 (2019).
- ³¹Z. Han, D. Ren, and D. Burghoff, "Sensitivity of SWIFT spectroscopy," *Opt. Express* **28**, 6002–6017 (2020).
- ³²A. Forrer, L. Bosco, M. Beck, J. Faist, and G. Scalari, "RF injection of THz QCL combs at 80 K emitting over 700 GHz spectral bandwidth," *Photonics* **7**, 9 (2020).
- ³³B. Schneider, F. Kapsalidis, M. Bertrand, M. Singleton, J. Hillbrand, M. Beck, and J. Faist, "Controlling quantum cascade laser optical frequency combs through microwave injection," *Laser Photonics Rev.* **15**, 2100242 (2021).
- ³⁴A. Forrer, M. Franckić, D. Stark, T. Olariu, M. Beck, J. Faist, and G. Scalari, "Photon-driven broadband emission and frequency comb RF injection locking in THz quantum cascade lasers," *ACS Photonics* **7**, 784–791 (2020).
- ³⁵E. Önder, D. O. Winge, M. Franckić, A. Forrer, U. Senica, G. Scalari, and A. Wacker, "Frequency modulations due to domain dynamics in terahertz quantum cascade lasers," *J. Appl. Phys.* **133**, 123101 (2023).
- ³⁶Y. Wang and A. Belyanin, "Active mode-locking of mid-infrared quantum cascade lasers with short gain recovery time," *Opt. Express* **23**, 4173–4185 (2015).
- ³⁷C. Silvestri, X. Qi, T. Taimre, and A. D. Rakić, "Multimode dynamics of terahertz quantum cascade lasers: Spontaneous and actively induced generation of dense and harmonic coherent regimes," *Phys. Rev. A* **106**, 053526 (2022).
- ³⁸A. Hugi, R. Maulini, and J. Faist, "External cavity quantum cascade laser," *Semicond. Sci. Technol.* **25**, 083001 (2010).
- ³⁹G. Wysocki, R. F. Curl, F. K. Tittel, R. Maulini, J.-M. Bulliard, and J. Faist, "Widely tunable mode-hop free external cavity quantum cascade laser for high resolution spectroscopic applications," *Appl. Phys. B* **81**, 769–777 (2005).
- ⁴⁰C. A. Curwen, J. L. Reno, and B. S. Williams, "Terahertz quantum cascade VECSEL with watt-level output power," *Appl. Phys. Lett.* **113**, 011104 (2018).
- ⁴¹Y. Wu, C. A. Curwen, M. Shahili, J. L. Reno, and B. S. Williams, "RF injection locking of THz metasurface quantum-cascade VECSEL," *Laser Photonics Rev.* **2023**, 2300007.
- ⁴²M. A. Kainz, S. Schönhuber, A. M. Andrews, H. Detz, B. Limbacher, G. Strasser, and K. Unterrainer, "Barrier height tuning of terahertz quantum cascade lasers for high-temperature operation," *ACS Photonics* **5**, 4687–4693 (2018).
- ⁴³A. Demić, Z. Ikonić, P. Dean, and D. Indjin, "Dual resonance phonon-phonon-terahertz quantum-cascade laser: Physics of the electron transport and temperature performance optimization," *Opt. Express* **28**, 38788–38812 (2020).
- ⁴⁴M. Franckić and J. Faist, "Bayesian optimization of terahertz quantum cascade lasers," *Phys. Rev. Appl.* **13**, 034025 (2020).
- ⁴⁵A. Demić, Z. Ikonić, P. Dean, and D. Indjin, "Prospects of temperature performance enhancement through higher resonant phonon transition designs in GaAs-based terahertz quantum-cascade lasers," *New J. Phys.* **24**, 033047 (2022).
- ⁴⁶V. Rindert, E. Önder, and A. Wacker, "Analysis of high-performing terahertz quantum cascade lasers," *Phys. Rev. Appl.* **18**, L041001 (2022).
- ⁴⁷C. Walthers, M. Fischer, G. Scalari, R. Terazzi, N. Hoyler, and J. Faist, "Quantum cascade lasers operating from 1.2 to 1.6 THz," *Appl. Phys. Lett.* **91**, 131122 (2007).
- ⁴⁸M. Wienold, B. Röben, X. Lü, G. Rozas, L. Schrottke, K. Biermann, and H. T. Grahn, "Frequency dependence of the maximum operating temperature for quantum-cascade lasers up to 5.4 THz," *Appl. Phys. Lett.* **107**, 202101 (2015).